IOP Publishing 2D Mater. 4 (2017) 025017 doi:10.1088/2053-1583/aa57ff

2D Materials

RECEIVED
12 September 2016

REVISED
3 December 2016

ACCEPTED FOR PUBLICATION
6 January 2017

PUBLISHED
1 February 2017

PAPER

Evolution of the size and shape of 2D nanosheets during ultrasonic fragmentation

Andrea Liscio[1,2], **Konstantinos Kouroupis-Agalou**[1,3], **Xavier Diez Betriu**[1], **Alessandro Kovtun**[1], **Emanuele Treossi**[1], **Nicola Maria Pugno**[4,5,6], **Giovanna De Luca**[7,8], **Loris Giorgini**[3] **and Vincenzo Palermo**[1]

[1] Istituto per la Sintesi Organica e la Fotoreattività - Consiglio Nazionale delle Ricerche (ISOF-CNR), via Gobetti 101, 40129 Bologna, Italy
[2] Istituto dei Sistemi Complessi - Consiglio Nazionale delle Ricerche (ISC-CNR), via del Fosso del Cavaliere 100, 00133 Roma, Italy
[3] Dipartimento di Chimica Industriale 'Toso Montanari', Università di Bologna, viale Risorgimento 4, 40100 Bologna, Italy
[4] Italian Space Agency, via del Politecnico snc, 00133 Roma, Italy
[5] Laboratory of Bio-inspired & Graphene Nanomechanics, Department of Civil, Environmental and Mechanical Engineering, University of Trento, Trento, Italy
[6] School of Engineering and Materials Science, Queen Mary University of London, Mile End Road, E1 4NS London, United Kingdom
[7] Dipartimento di Scienze chimiche, biologiche, farmaceutiche e ambientali, Università di Messina, viale Ferdinando Stagno d'Alcontres 31, 98166 Messina, Italy
[8] Istituto per i Polimeri Compositi e Biomateriali - Consiglio Nazionale delle Ricerche (IPCB-CNR), p.le E. Fermi 1, 80055 Portici (Napoli) Italy

E-mail: andrea.liscio@isc.cnr.it and vincenzo.palermo@isof.cnr.it

Keywords: graphene oxide, metrology, scanning probe microscopy, surface science

Supplementary material for this article is available online

Abstract

2-dimensional (2D) nanosheets such as graphene, graphene oxide, boron nitride or transition metal dichalcogenides can be produced on a large scale by exfoliation techniques. The lateral shape of these 2D materials is typically considered random and irregular, and their average size is often estimated using techniques characterized by strong approximations or poor statistical significance. Here we measure in a quantitative, objective way the size and shape of 2D monoatomic nanosheets using a combination of optical, electronic and scanning probe techniques. We measure, one by one, the size and shape of thousands of sheets of graphene oxide as they undergo a standard ultrasonication treatment. Using automatic image processing and statistical modelling we identify two different fragmentation processes in 2D at the nanoscale, related to two populations of nanosheets described by gamma and exponential size distributions respectively. The two populations of sheets coexist during the fragmentation process, each one retaining its average size and shape. Our results explain the size reduction commonly observed in nanosheets upon sonication as an effect of changes in the respective weights of the two populations of nanosheets present in the material.

1. Introduction

In recent years, 2D materials (such as graphene, boron nitride and transition metal dichalcogenides) have attracted increasing attention for a wide range of possible applications, from electronics, to composites, to biology [1, 2].

However, the lack of a clear metrology and quality control is creating confusion among industrial end-users, with many websites and companies selling what should be called graphite powders or thin platelets, rather than graphene. Despite the nomenclature [3] and classification framework [4] that have been proposed for 2D graphene-based materials, a clear agreement on metrology and standards is still missing.

Unlike other nano-materials, graphene can be produced by several methods, either using top-down or bottom-up approaches, leading to a wide range of graphene-based 2D materials with very different quality and cost. For example, high-shear [5] or electrochemical [6] exfoliation techniques, yielding stable solutions in aqueous and organic solvents, have recently been upscaled from lab to industrial production level.

The final quality of graphene-based solutions and powders depends on a combination of complex processes, including bubble cavitation, shear forces and intercalation, as well as possible chemical oxidation of the pristine graphite. In previous work, we studied the mechanism of how graphene nanosheets detach from bulk graphite upon ultrasonication, comparing this process with (more damaging) chemical or electrochemical exfoliation [7]. After detaching from graphite, the nanosheets continue to be broken and fragmented in solution, due to the presence of ultrasonic waves. An understanding of the physics of such fragmentation processes is important to optimize the production rate of 2D materials with pre-programmed, well-defined and tunable chemico-physical properties.

Standardized approaches to study and describe 2D nanosheets are thus urgently needed, because both fundamental studies and industrial applications require controlled, reproducible properties of the material.

In particular, the size of 2D materials is a fundamental parameter to be estimated because it has an impact on their performance, influencing mechanical and electrical properties in polymer composites [8], charge transport [9], gas permeation in thin films [10] and even biological activity [11].

Here we show that a quantitative study of the nanosheets' size and shape distribution can be done combining statistical, mathematical and physical tools, thus providing detailed information on the physical properties of 2D materials and the dynamics of the mechanisms involved in their production. We describe an analysis technique suitable to characterize large amounts of nanosheets providing robust statistical parameters to describe them. This analysis allows us to define and use a single, scalar quantitative parameter to characterize the areal dispersion of such 2D materials.

Our approach is inspired by the chemists from the first half of the 20th century, who were challenged to find new techniques to produce, characterize and define 1D polymers [12]. One century later, we face similar challenges in producing and characterizing a new class of materials, formed by repeating units not in one but in two dimensions [13], obtained by fragmentation of bulk graphite.

For linear polymeric chains, the molecular weight unambiguously identifies the 1D length of the object. The metrology of 2D materials is however more complex, because exfoliation yields a poly-dispersed range of nanosheets featuring not only a wide range of sizes, but also different shapes. In all works previously published on this topic, the only morphological parameter reported is the lateral size, quantified using two common statistical parameters: arithmetic mean and standard deviation (SD), assuming that the nanosheets' length follows a Gaussian distribution. However, all published experimental data show that, for any given 2D material the size distribution is non-Gaussian, skewed and highly asymmetric [1, 14]. Noteworthy, this skewed distribution is a general statistical feature that appears in almost all areas of science, e.g. the length distribution of polymers, the content of chemical elements in rocks, the abundance of species in biology and the distribution of galaxies in astronomy [15].

Therefore we decided to perform extensive statistical measurements of 2D nanosheets obtained in solution, using microscopic techniques and automatic image processing to extract robust statistical data about the size and shape of these sheets.

We demonstrated the validity of this approach using a standard 2D material as the target system, i.e. graphene oxide (GO) completely exfoliated without any aggregation, featuring more than 99% of monoatomic nanosheets in water [9, 16]. We monitored the evolution of the size of the nanosheets as they underwent a standard ultrasonication treatment from 0 to 100 h. The sheets, spanning a wide size range from 100 μm down to 10 nm (figure 1), were then deposited on ultra-flat silicon substrates and measured using a combination of different microscopy techniques: optical fluorescence microscopy (FM) [16], scanning electron microscopy (SEM) and atomic force microscopy (AFM). The images obtained were then analyzed by an image processing software, which allowed the measurement of the size and 2D shape of all the sheets produced, one by one (see SI (stacks.iop.org/TDM/4/025017/mmedia)). Even though the three techniques used rely on different physical processes (probing the sample with photons, electrons or a microscopic sharp tip), we could use our analysis procedure in the same way on all collected images.

We could, in this way:

- analyze a statistically representative sample of the GO nanosheets, corresponding to more than 2500 sheets for each sample;
- follow the evolution of size and shape distribution of the nanosheets during the fragmentation process;
- fit these data using different mathematical models of dynamic fragmentation [17],
- deduce the underlying fragmentation mechanisms acting on different length scales and
- using the experimental data, select a robust parameter to quantify the heterogeneity of the 2D system studied.

2. Sample preparation and experimental methods

Single-layer GO sheets were obtained by oxidation and exfoliation of graphite using the modified Hummers method [16]. The prepared GO suspensions in water are stable for more than 1 year as confirmed by UV–vis absorption measurements. The fragmentation of GO sheets was obtained by sonicating the suspensions for up to 100 h with an Elmasonic P 70 H ultrasonic cleaning unit ($W_{\text{output}} = 120$ W, freq $= 37$ kHz) (see SI: experimental methods).

AFM was used to monitor the abundance of single layers (>99%) by spin coating the solution (conc $= 0.1$ g l^{-1}) on an ultra-flat silicon oxide surface. GO sheets were deposited with negligible overlap (<5%) [9] on silicon spanning a wide size range from 100 μm down to 10 nm and examined combining three microscopic techniques: FM, SEM and AFM.

FM is based on the interaction of the nanosheets with fluorescent molecules, as previously described in [16]. SEM and AFM were performed with standard commercial setups (see supporting information).

Image processing and analysis was performed using commercial software (SPIP™ version 6.6.1) able to detect the different sheets by contrast threshold and

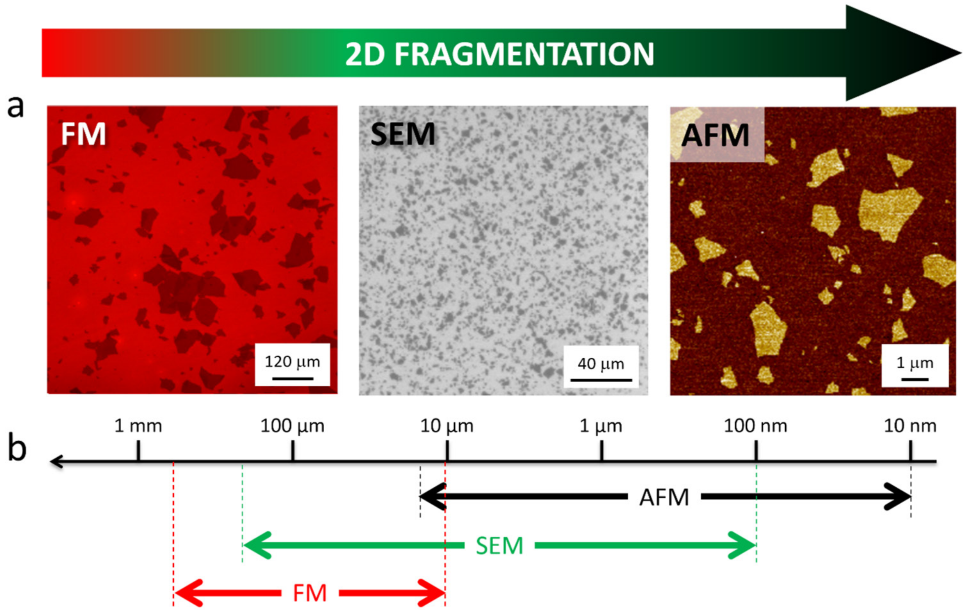

Figure 1. (a) FM, SEM and AFM images of GO sheets deposited on a silicon substrate. Total surface areas sampled using the three techniques: 60 mm^2, 0.1 mm^2 and 0.01 mm^2. (b) A scheme showing the different length-scales explored with the different techniques.

contour analysis [18] (see SI: Image processing, for details on image flattening and detection algorithm).

The statistical analysis of the discrete variables acquired by the automatic image processing was performed by testing continuous distributions commonly used in fragmentation models: inverse power, log-normal, gamma and exponential functions. The discrimination between different functions was performed by analyzing the distribution itself as well as the corresponding complementary cumulative distribution. The best-fit functions were obtained using the Levenberg–Marquardt algorithm (see SI: Mathematical methods).

3. Results and discussion

3.1. How to describe the morphology of a 2D material

In previous works on exfoliation, the geometrical properties of 2D materials were described only by the lateral size, which was typically obtained by analyzing few tens of sheets with transmission electron microscopy (TEM). From the experimental point of view, this approach is tedious and prone to artifacts, given that the operator arbitrarily chooses the longest axis of the sheet as a definition of its lateral size.

A sheet with a given area can have a square shape or conversely be long and thin. In a similar way, a sheet with a long axis of given length can be square, or elongated, or simply irregular. Thus, 2D objects with variable shape cannot be defined by a single scalar number, neither length nor area. In general, also the shape of objects plays a crucial role in affecting the rheology of carbon nanoparticle suspensions and nanocomposites [19] or the percolation threshold in networks of shaped objects [20].

We thus describe a GO sheet using different parameters related to their area and their shape. The analysis of the shape of 2D objects is not trivial and several dimensionless parameters are currently used in image analysis to measure shapes [21].

We chose to use the form factor, a standard morphological parameter calculated from the sheet area (A) and perimeter (p), to describe the irregularity of the shape respect to a circle: FF $= 4\pi A/p^2$. For comparison, we also used another widespread morphological parameter (aspect ratio) which describes the anisotropy of the shape (see supporting info).

Once the shape is fixed, either area or length could be used to describe the object; we chose to report the area distribution rather than the length distribution because measuring the length of an irregular object is somehow arbitrary (the operator has to choose subjectively the longest axis). Conversely, the area of each sheet shall be measured objectively, pixel by pixel, by the software we used [22].

We considered these nanosheets as non-stretchable materials where elastic deformations are negligible. Geometrically, this corresponds to the case in which the surface metric structure is locally Euclidean. Hence, GO sheets can move and bend in solution without any change in their surface area or shape, which are intrinsic properties of the sheet.

3.2. Statistical analysis of the nanosheet average area and size

By analyzing FM, SEM and AFM images, we evaluated the mean values of the chosen morphological parameters for different sonication times. Figure 2 shows the evolution with time of average area and shape (quantified as the form factor defined above). Error bars correspond to the calculated SD. All three techniques gave an excellent agreement, showing that there were none of the systematic errors typical of

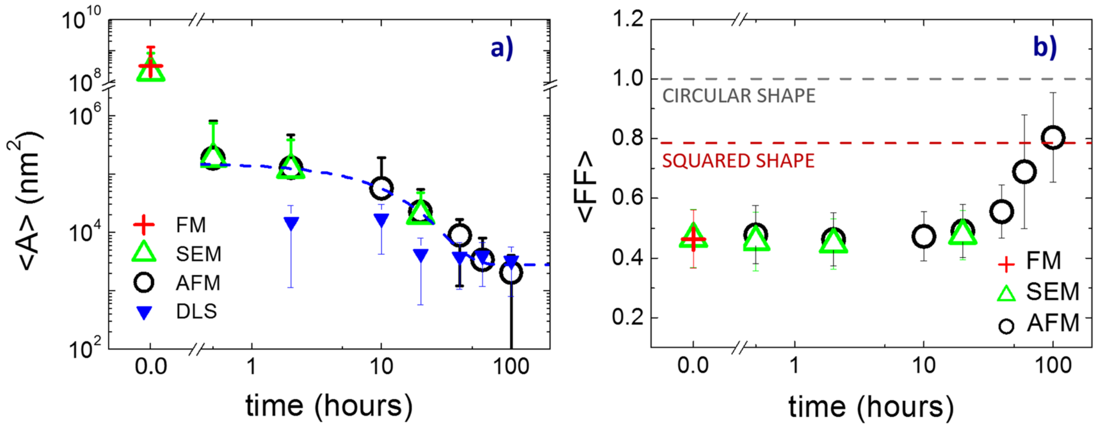

Figure 2. (a) Area and (b) shape evolution of the fragments in function of sonication time directly obtained by (+) FM, (△) SEM, (○) AFM and (▼) DLS. In (a) the blue dashed line shows an exponential fit of the FM, SEM and AFM data points. In (b) the Form factor (FF) is reported, as a measure of shape (see main text). Grey (red) dashed line corresponds to the ideal Form Factor of a circular (square) shaped object.

subjective, manual image analysis, thus demonstrating that different microscopies can be fruitfully combined to probe the sheet populations within a range spanning over six orders of magnitude, from 10^9 to 10^3 nm^2 [21].

A similar trend, but consistently lower $\langle A\rangle$ values, was achieved using a macroscopic averaging technique, dynamic light scattering (DLS). Although DLS provides a fast measurement by probing macroscopic volumes of solution, the data analysis assumes that the measured objects have a 3D spherical shape [23]. A semi-quantitative method to model DLS of 2D nanosheets was previously developed, assuming an infinite rigidity of the dispersed sheets [24]. However, the bending of nanosheets in solution cannot be neglected because folding is energetically more favorable than a perfectly flat sheet [25]. This causes an intrinsic underestimation of the measured size using DLS, especially for large sheets that are more likely to fold. For this reason, the data reported hereafter are obtained from one-by-one analysis of single sheets on substrates, thus avoiding any underestimation due to ensemble averaging typical of DLS or other bulk, macroscopic measurements.

The value $\langle A\rangle \approx 4 \times 10^8$ nm^2 measured for pristine GO at $t = 0$ (corresponding to an average lateral size $\sqrt{A}$ of ~20 μm) decreased to $\langle A\rangle \approx 1.6 \times 10^5$ nm^2 after half an hour of sonication. Thereafter the area continued to slowly decrease, roughly following an exponential trend (dashed line in figure 2(a)). This gradual reduction in size upon sonication is well known, having been commonly observed in all works on the production of 2D materials, and indicates that fragmentation is a scaling process based on random scissions, without variation in the shape of the fragments (see [26, 27], section 5 and figure S12 in supporting info).

However, a change in the shape parameter $\langle \mathrm{FF}\rangle$ is clearly observed in our case after $t = 40$ h (figure 2(b)).

To solve this inconsistency, we studied in detail not only the average area, but also how the sheet areas differ within each sample.

3.3. Analysis of area and size distribution in each sample

The analysis of the area distribution (f_A) of each sample (figure 3) revealed more details on the evolution of the material upon fragmentation.

For the initial GO suspension, f_A was linear in log–log scale (figure 3(a)), indicating a scale-invariant fractal behavior with dimension $D = 1.0 \pm 0.1$ [28]. A scale-invariant area distribution indicates that the initial population can be described in terms of a Smith–Volterra–Cantor set [29] and that the GO exfoliation from bulk graphite proceeds with iterative self-similar steps where the fragmentation mechanism only depends on the details of the chemical exfoliation process, including intercalation of graphite and formation of gas bubbles [7].

After half an hour of sonication the pristine linear trend was still present (figure 3(b)); however, some deviations from linearity were observed for the smaller fragments.

After $t = 2$ h, f_A changed significantly (figure 3(c)) with the best fit now obtained using a Gamma distribution which becomes predominant after 10 and 20 h (figures 3(d) and (e)). Gamma distributions are typical of random fragmentation models that follow 2D-Voronoi tessellation [26, 30], similar to fragmentation of brittle materials (a.k.a. 'bulk fragmentation'), such as ceramics, glassware and rocks. Such tessellation produces fragments with similar shapes; this process can be explained by mechanical failure of GO sheets due to their structure composed of graphene-like, sp^2-hybridized patches divided by highly-defective sp^3 regions [31], where crack propagation shall start [32].

Between 40 and 60 h of sonication (figures 3(f) and (g)) we observed the coexistence of two populations: one consisting of large sheets following a Gamma distribution (called hereafter population P_G), and the other of small-sized sheets following an exponential distribution (P_E).

After $t = 100$ h (figure 3(h)) only population P_E was observed. The exponential distribution indicates the pres-

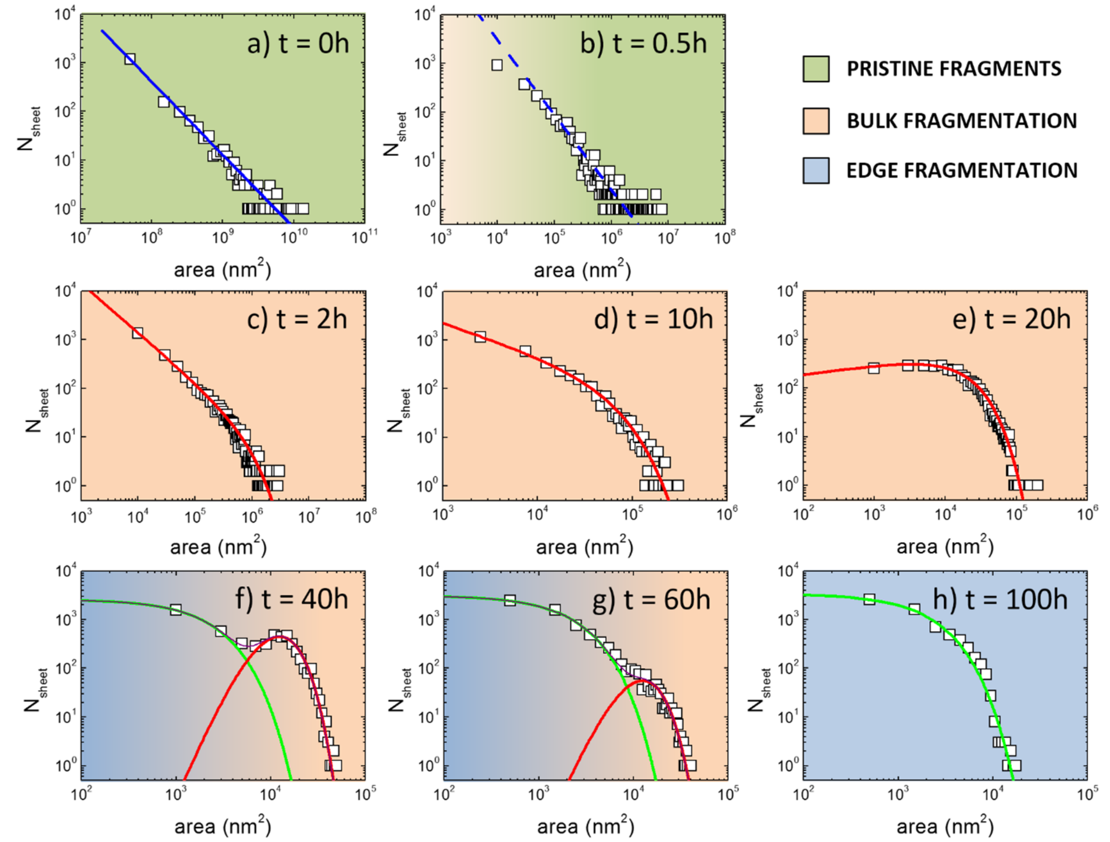

Figure 3. Evolution of size distribution of the 2D nanosheets ((a)–(h)) for different sonication times. The number of sheets (N_{sheet}) versus sheet area is plotted in log–log scale, from 0 h to 100 h. The measured distributions are fitted by: (blue) power law, (red) Gamma and (green) exponential functions. Light green, light yellow and light blue backgrounds indicate different active regimes: pristine fragments, bulk fragmentation and edge fragmentation.

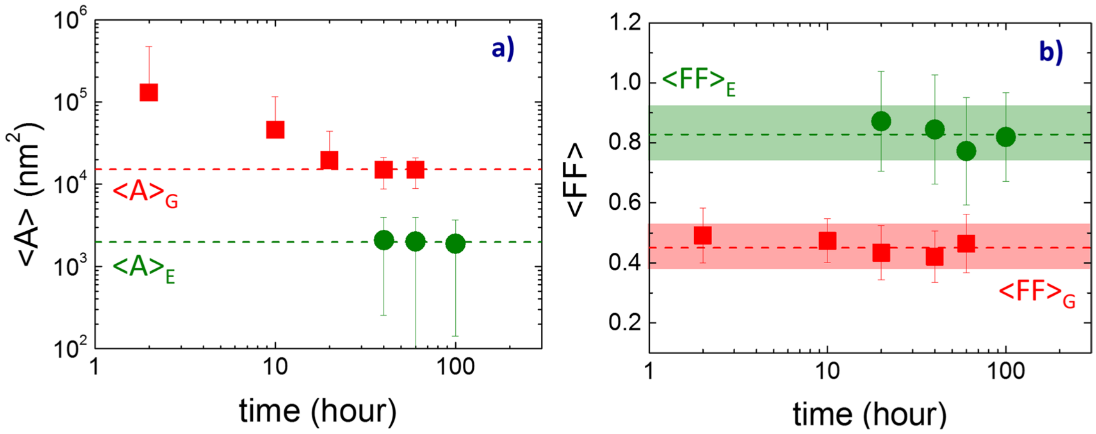

Figure 4. Time-evolution of (a) area and (b) shape, as measured by the form factor (FF) monitoring the two populations: P_G (red squares) and P_E (green circles). $\langle A\rangle_G$ and $\langle A\rangle_E$ are the asymptotic area values of the two populations. Dashed lines correspond to the mean values: $\langle \mathrm{FF}\rangle_G$ and $\langle \mathrm{FF}\rangle_E$. Shadowed areas are centered to the corresponding average values of the shape parameters (dashed lines) and the widths correspond to twice the standard deviation (=2·SD).

ence of a fragmentation process starting from seed defects on the outer edges of the sheets [33], from which crack lines depart (figure S13). This mechanism can be depicted as some kind of edge (a.k.a. coastal) erosion (see SI).

The time-evolution of average area $\langle A\rangle$ of the two separated populations is summarized in figure 4(a). P_G sheets fragmented until they reached an asymptotic area $\langle A\rangle_G = 15 \pm 6 \times 10^3$ nm^2 while P_E sheets had a smaller area $\langle A\rangle_E = 2 \pm 1 \times 10^3$ nm^2 that was no longer modified by sonication.

This approach, based on the separate analysis of P_G and P_E, allows us to confirm that the shape of the sheets is fairly constant during the whole fragmentation process. Figure 4(b) shows that the large sheets P_G have a quite constant form factor (FF) of 0.45 ± 0.06 while P_E are more isotropic, with values of 0.83 ± 0.09.

The form factors, and thus the shape regularity of the two populations remain constant upon fragmentation, in agreement with [26]; thus, the change in ⟨FF⟩ observed in figure 2(b) is not due to a change in the shape of the sheets, but simply to a change in the respective weights of the two populations, with the number of P_G decreasing in time due to fragmentation, eventually disappearing and leaving only P_E sheets in solution.

To confirm that this behavior was not due to the particular parameter used to measure shape, we performed a similar analysis using another widely used morphological parameter (aspect ratio) which describes the anisotropy of the shape, obtaining the same results (see section 3 and figure S9 in supporting info).

In general, physical models that do not take into account the presence of two distinguished sheet populations failed to describe the fragmentation process. Incoherencies are observed if the sheet area is described in the conventional way, using mean and SD, which cannot account for the contribution of different populations in the sample. These parameters can give a correct statistical description of the sample only when f_A is Gaussian. Instead, their use can cause misleading results when comparing distributions with different skew and shape.

Overall, a detailed analysis of how the area and shape of the nanosheets evolved during fragmentation indicates that two different processes acted on different scales. Large sheets P_G were broken down by fracture events that divided each sheet into pieces with a comparable shape described by a Gamma distribution and reaching the asymptotic value $\langle A\rangle_G$ corresponding to the ultimate fragments area obtained by 'bulk fragmentation' of the pristine material. Following this stage, a second fragmentation process became relevant, where small pieces were cut from the edges of the larger sheets by an erosion process, creating a new population of objects described by an exponential distribution, having a smaller and constant area $\langle A\rangle_E$. Each populations had a different shape that was not modified by sonication, P_E sheets being systematically more isotropic with respect to P_G, due to the erosion process.

These results cast new light on the commonly observed fragmentation process of nanosheets with sonication [10, 34]. The decrease of area is not due to a continuous shrinkage that affects all the sheets in the same way, but rather to a change in the ratio of two populations of sheets created by two different physical mechanisms.

We underline that the thickness of GO sheets as well as their chemical composition were constant throughout the entire fragmentation process, as monitored by AFM, x-ray photoemission spectroscopy (XPS) and zeta-potential measurements (figures S10 and S11). The mechanical stress due to the sonication did not create new oxidized defects in the GO sheets and the fractures propagated along already existing defects. The two different mechanisms observed are thus not due to presence of different chemical defects in the initial or later stages, but rather to a change in the physical process of fragmentation while the average sheet size was shrinking.

3.4. Influence of sheet area on mechanical properties

During GO sonication, cavitation shatters the large sheets (P_G) creating cracks that propagate from their edges and become unstable, giving rise to side branches, which can merge to form additional (small) fragments, observed as the P_E population. The onset of two populations of larger and smaller fragments has previously been observed experimentally in 1D, e.g. in the fragmentation of spaghetti [35] (a problem that fascinated also Nobel laureate R Feynman) and 3D (e.g. in blasting of rocks) but only predicted by theoretical models for 2D systems [36].

The fragmentation action in a typical sonication treatment is based on the implosion of micro-bubbles created by ultrasound cavitation process. Collapsing at super-sonic speed, these bubbles break down the sheets due to shear viscous forces that cause mechanical stress [37]. The asymptotic area of fragments thus generated ($\langle A\rangle_G$) corresponds to the smallest surface on which the viscous stress shall act to break the fragment further.

Thus we used the experimental value found for the smallest average area to estimate the mechanical strength of single nanosheets. In terms of Mott statistical theory [33], we extended a 1D model, previously used for carbon nanotubes [38], to the 2D case (see SI). $\langle A\rangle_G$ and the viscous stress applied by cavitation bubbles were used as input in the model, obtaining a fracture strength of P_G sheets of 30 ± 10 GPa, which is in good agreement with estimations from previous modelling [39] and experimental [40] works.

The results presented here demonstrate the complexity of fragmentation in 2D, highlighting that it is not correct to quantify the physical properties of an ensemble of sheets with the most widely-used pair of statistical parameters (i.e. mean and standard deviation). However, the definition of a robust statistical indicator could be useful to describe the uniformity of these materials and to compare them with others.

3.5. A new quantitative approach to measure the heterogeneity of 2D materials in solution

Graphene can be viewed as a polymer consisting of atoms covalently tethered in 2D [41]. Therefore, we propose to extend to 2D objects concepts already developed, one century ago, for 1D polymers. The description of the molecular mass of a polymer is determined by the mass-molar dispersity ($Đ_M$) [42] which is commonly used for quantitative analysis of static light scattering measurements (SLS), viscometry and size exclusion chromatography [43]. Also known as polydispersity index, $Đ_M$ quantifies the variability in length of the polymer chains, and is defined as the weight-averaged molecular weight (M_w) divided by the number-averaged molecular weight (M_n).

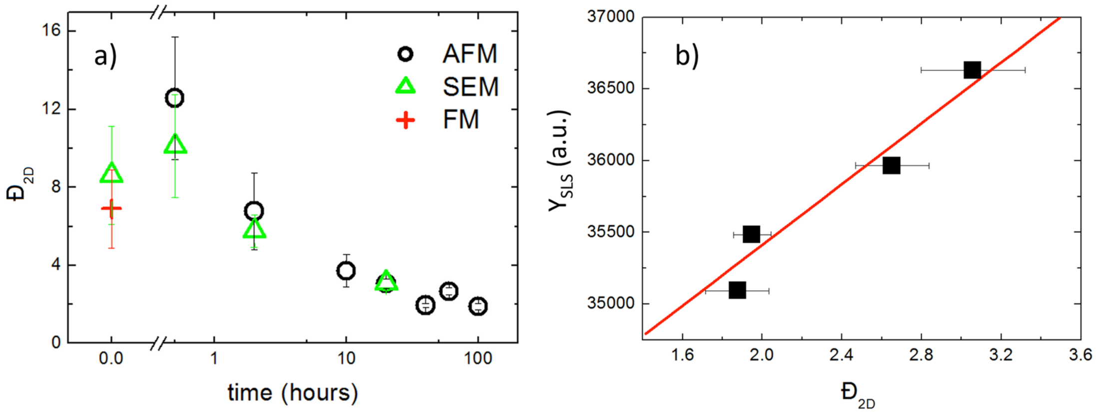

Figure 5. Experimental measurements of 2D areal dispersity index. (a) Time-dependence of areal dispersity $Đ_{2D}$ measured with different techniques. (b) Experimental evidence of the correlation between SLS signal (black squares) and $Đ_{2D}$ for $t > 20$ h. The red line is a linear fit of the experimental data.

Taking into account that the mass of 2D objects is directly proportional to the area (A), we thus extended the validity of $Đ_{M}$ by defining the area dispersity of 2D materials ($Đ_{2D}$) as:

$$Đ_{2D} = \frac{M_w}{M_n} = \frac{A_w}{A_n} = \frac{\sum f_A \cdot A^2}{\sum f_A \cdot A} \times \frac{N_{TOT}}{\sum f_A \cdot A} = \frac{\langle A^2 \rangle}{\langle A \rangle^2} \quad (1)$$

resulting in the mean value of the squared area ($\langle A^2 \rangle$) divided by the square of the mean value of the area ($\langle A \rangle^2$). Figure 5(a) plots the time evolution of $Đ_{2D}$ of GO sheets during sonication. In the first half hour the dispersity increased indicating a higher heterogeneity of the solution due to the persistence of unbroken pristine material, as discussed before. Afterwards, with continuing sonication $Đ_{2D}$ reduced reaching a value close to 2 ascribable to the P_E dispersity.

Finally, we tested the validity of this parameter demonstrating how it can explain some macroscopic property of the material studied. In analogy with 1D polymers, dispersity variation influences the way that light is scattered by 2D objects in solvent. We studied the GO suspension with SLS measurements, which are commonly used to characterize polymers and colloidal solutions. At low particle concentrations and for Rayleigh scattering, the SLS signal is proportional to the ratio between M_w and the z-averaged mean-square radius of gyration [44], and can be written as a linear function of $Đ_{2D}$, taking into account equation (1):

$$Y_{SLS} = \alpha + \beta \cdot \frac{M_w}{\langle R_g^2 \rangle_z} = \alpha + \beta \cdot \frac{A_n}{\langle R_g^2 \rangle_z} \cdot \frac{A_w}{A_n} = \alpha + \beta \cdot \frac{A_n}{\langle R_g^2 \rangle_z} \cdot Đ_{2D} \quad (2)$$

where α and β represent dimensional and proportional parameters.

The linear trend achieved for $t \geqslant 20$ h (figure 5(b)) indicates that the ratio $\langle A \rangle / \langle R_g^2 \rangle_z$ is constant, confirming the validity of using the $Đ_{2D}$ index for 2D materials. This evidence suggests that the smallest GO sheets produced by long sonication times had no relevant folding in water suspensions, behaving as quasi-planar objects, in agreement with the DLS measurements.

4. Conclusions

Fragmentation can be described as the process of disintegrating an object by multiple fracturing events. The physics of fragmentation is of interest in different fields of science and engineering: materials science, failure analysis and even astronomy. The analysis of the size distribution obtained with a given fragmentation process allows us to understand the underlying physics of that process. As example, using this approach Brown *et al* [45] studied the size distribution of many galaxies, demonstrating that the universe underwent a single fragmentation event separating into protogalactic volumes at a relatively early stage after the Big Bang. In most cases, the study of size distribution is performed on 3D objects (i.e. powders or rocks from mining activities) or on 1D polymers. Here we performed, for the first time, such an analysis on a purely 2D material. While polymers can be analyzed only at the ensemble level, one of the most striking features of graphene and related 2D materials is that even single sheets can be easily observed with high-throughput microscopy techniques. Thus, they are an ideal material to combine analysis from macro scale to the single sheet, allowing monitoring of chemico-physical processes at the nanoscale.

We underline that it was possible to obtain statistically sound data on all the different sheet populations thanks only to the good quality of the material chosen (GO sheets), whose typical lateral size matches the ideal working range of the selected microscopic techniques very well. Contrary to previous works, the changes in area observed could be ascribed only to 2D fragmentation, not to exfoliation of 3D objects (e.g. graphene multilayers) into 2D nanosheets. This is because the original starting material we chose was already a purely 2D material, thus ruling out any influence of 3D processes on the changes in sheet population.

This approach can be applied to all the 2D materials having topological defects (very few atoms holes), small holes (few nm), fissures, etc., with size significantly smaller than the sheet size. Until defect size is much smaller than sheet size, this will just affect the average fracture strength, but will not change the fragmentation mechanism.

In summary, we described a new protocol for the quantitative analysis at the nano- and micro-scale of fragmentation in two dimensions. The results obtained allow some ambiguities reported in literature to be solved: by showing the coexistence of different GO populations, we demonstrated that the GO suspensions can be described as a blend of large sheets and small debris fragments (similar to fulvic oxides), casting new light on the results recently reported on this topic [46].

The proposed approach, based on measurement and calculation of areal dispersity, builds on methods already well-established for 1D polymers, and could allow a rigorous metrology and a reliable, objective quality control of graphene-like materials for both fundamental and applied research, accelerating the use of these new, exciting materials in industrial applications.

Acknowledgment

We thank Dr Meganne Christian for her comments on the manuscript. The research leading to these results has received funding from the European Union Horizon 2020 Framework Programme under grant agreement n°696656 Graphene Core1 and the EC Marie-Curie ITN-iSwitch (GA no. 642196). NMP is also supported by the European Research Council PoC 2015 "Silkene" No. 693670, by the European Commission H2020 with the Fet Proactive "Neurofibres" No. 732344.

Supporting information is available free of charge via the Internet at http://pubs.acs.org.

Author contributions

AL and VP conceived the experiments and wrote the manuscript. KKA, XDB, AK, ET and GDL performed sample preparation and characterization. NMP and LG contributed to data analysis. NMP derived the model to quantify the GO mechanical resistance. All authors have given approval to the final version of the manuscript.

References

[1] Coleman J N *et al* 2011 *Science* **331** 568–71

[2] Ferrari A C *et al* 2015 *Nanoscale* **7** 4598–810
Novoselov K S, Fal'ko V I, Colombo L, Gellert P R, Schwab M G and Kim K 2012 *Nature* **490** 192–200

[3] Bianco A *et al* 2013 *Carbon* **65** 1–6

[4] Wick P *et al* 2014 *Angew. Chem., Int. Ed.* **53** 7714–8

[5] Paton K R *et al* 2014 *Nat. Mater.* **13** 624–30

[6] Parvez K, Wu Z-S, Li R, Liu X, Graf R, Feng X and Müllen K 2014 *J. Am. Chem. Soc.* **136** 6083–91

[7] Xia Z Y, Pezzini S, Treossi E, Giambastiani G, Corticelli F, Morandi V, Zanelli A, Bellani V and Palermo V 2013 *Adv. Funct. Mater.* **23** 4684–93

[8] De S, King P J, Lyons P E, Khan U and Coleman J N 2010 *ACS Nano* **4** 7064–72
Valles C, Abdelkader A M, Young R J and Kinloch I A 2014 *Faraday Discuss.* **173** 379–90

[9] Liscio A, Veronese G P, Treossi E, Suriano F, Rossella F, Bellani V, Rizzoli R, Samorì P and Palermo V 2011 *J. Mater. Chem.* **21** 2924–31

[10] Guo F, Silverberg G, Bowers S, Kim S-P, Datta D, Shenoy V and Hurt R H 2012 *Environ. Sci. Technol.* **46** 7717–24

[11] Russier J, Treossi E, Scarsi A, Perrozzi F, Dumortier H, Ottaviano L, Meneghetti M, Palermo V and Bianco A 2013 *Nanoscale* **5** 11234–47

[12] Mülhaupt R 2004 *Angew. Chem., Int. Ed.* **43** 1054–63

[13] Palermo V 2013 *Chem. Commun.* **49** 2848–57

[14] Kouroupis-Agalou K, Liscio A, Treossi E, Ortolani L, Morandi V, Pugno N M and Palermo V 2014 *Nanoscale* **6** 5926–33

[15] Limpert E, Stahel W A and Abbt M 2001 *Bioscience* **51** 341–52

[16] Treossi E, Melucci M, Liscio A, Gazzano M, Samorì P and Palermo V 2009 *J. Am. Chem. Soc.* **131** 15576

[17] Zhang F 2009 *Shock Wave Science and Technology Reference Library* (New York: Springer)

[18] Liscio A 2013 *Chemphyschem* **14** 1283–92

[19] Cassagnau P 2015 *Rheology of Non-Spherical Particle Suspensions* ed G Ausias (Betlin: Springer) pp 59–75

[20] Mertens S and Moore C 2012 *Phys. Rev.* E **86** 061109

[21] Russ J C and DeHoff R T 2000 *Practical Stereology* 2nd edn (New York: Academic)

[22] Gray A 1993 *Modern Differential Geometry of Curves and Surfaces* (Boca Raton, FL: CRC Press)

[23] Goncalves G, Vila M, Bdikin I, de Andres A, Emami N, Ferreira R A S, Carlos L D, Gracio J and Marques P A A P 2014 *Sci. Rep.* **4** 6735

[24] Lotya M, Rakovich A, Donegan J F and Coleman J N 2013 *Nanotechnology* **24** 265703

[25] Schniepp H C, Kudin K N, Li J L, Prud'homme R K, Car R, Saville D A and Aksay I A 2008 *ACS Nano* **2** 2577–84

[26] Bertoin J 2001 *Probab. Theory Relat.* **121** 301–18

[27] Krapivsky P L and Bennaim E 1994 *Phys. Rev.* E **50** 3502–7

[28] Turcotte D L 1986 *J. Geophys. Res.* **91** 1921–6

[29] Falconer K J 2003 *Fractal Geometry: Mathematical Foundations and Applications* 2nd edn (Chichester: Wiley)

[30] Okabe A, Boots B N and Sugihara K 1992 *Spatial Tessellations: Concepts and Applications of Voronoi Diagrams* (Chichester: Wiley)

[31] Erickson K, Erni R, Lee Z, Alem N, Gannett W and Zettl A 2010 *Adv. Mater.* **22** 4467–72

[32] Palermo V, Kinloch I A, Ligi S and Pugno N M 2016 *Adv. Mater.* **28** 6232–8

[33] Grady D E 2010 *Int. J. Fract.* **163** 85–99

[34] Kucki M *et al* 2016 *Nanoscale* **8** 8749–60

[35] Audoly B and Neukirch S 2005 *Phys. Rev. Lett.* **95** 095505

[36] Åström J A, Ouchterlony F, Linna R P and Timonen J 2004 *Phys. Rev. Lett.* **92** 245506

[37] Hennrich F, Krupke R, Arnold K, Rojas Stütz J A, Lebedkin S, Koch T, Schimmel T and Kappes M M 2007 *J. Phys. Chem.* B **111** 1932–7

[38] Ahir S V, Huang Y Y and Terentjev E M 2008 *Polymer* **49** 3841–54

[39] Gomez-Navarro C, Weitz R T, Bittner A M, Scolari M, Mews A, Burghard M and Kern K 2007 *Nano Lett.* **7** 3499–503
Suk J W, Piner R D, An J H and Ruoff R S 2010 *ACS Nano* **4** 6557–64

[40] Cao C, Daly M, Singh C V, Sun Y and Filleter T 2015 *Carbon* **81** 497–504

[41] Kim J, Cote L J and Huang J X 2012 *Acc. Chem. Res.* **45** 1356–64

[42] Stepto R F T 2009 *Pure Appl. Chem.* **81** 351–3

[43] Rudin A and Choi P 2013 *The Elements of Polymer Science and Engineering* 3rd edn (Oxford: Elsevier)

[44] Geiduschek E P and Holtzer A 1958 *Adv. Biol. Med. Phys.* **6** 431–551

[45] Brown W K, Karpp R R and Grady D E 1983 *Astrophys. Space Sci.* **94** 401–12

[46] Rodriguez-Pastor I, Ramos-Fernandez G, Varela-Rizo H, Terrones M and Martin-Gullon I 2015 *Carbon* **84** 299–309
Rourke J P, Pandey P A, Moore J J, Bates M, Kinloch I A, Young R J and Wilson N R 2011 *Angew. Chem., Int. Ed.* **50** 3173–7
Thomas H R, Day S P, Woodruff W E, Valles C, Young R J, Kinloch I A, Morley G W, Hanna J V, Wilson N R and Rourke J P 2013 *Chem. Mater.* **25** 3580–8

Evolution of the size and shape of 2-dimensional nanosheets during ultrasonic fragmentation

Supporting information

1.EXPERIMENTAL METHODS

To monitor the sheet population from the meso- to the nano-scopic scale we used a combination of different techniques (fig. 1 in main text): optical fluorescence microscopy (FM),[1] scanning electron microscopy (SEM) and atomic force microscopy (AFM). In this way we could analyse more than 2,500 sheets for each sample. The total surface areas sampled using the three techniques were: 60 mm^2 (FM), 0.1 mm^2 (SEM) and 0.01 mm^2 (AFM).

FM

Images were taken in reflection mode with a Nikon Eclipse 80i optical microscope. The images were recorded with a digital color camera Nikon Coolpix 5400. Samples were prepared by spin-coating the GO sheets on 300 nm thick silicon oxide substrate that was covalently functionalised with triethoxysilane fluorescent thiophene-based dye, N-(3-(triethoxysilyl)propyl 2,2′:5′,2′′:5′′,2′′′-quaterthiophene-5-carboxamide, as described in ref. [1].

SEM–

Scanning electron microscopy (SEM) images were acquired using a FEI Dual Beam system (FIB-SEM) 235 with a 1 nm electron beam.

AFM

Atomic Force Microscopy (AFM) images were obtained in tapping mode with a commercial microscope (MultiMode Nanoscope IIIa, Bruker). The device was equipped with a J scanner, which was calibrated using the manufacturer’s grating. Ultrasharp tips (RTESPA MPP-11120, Silicon cantilevers, Bruker, typical force constant 40 N/m, resonant frequency 300 kHz) were used. Height images were flattened to remove background slopes. No other filtering procedures were performed on the images. AFM images were analysed using Spip^{TM} software. Detailed information about flattening procedures of the AFM images and the quantitative analysis using the frequency spectra can be found in Ref. [2].

XPS

X-ray photoelectron spectroscopy (XPS) spectra were recorded with a Phoibos 100 hemispherical energy analyser (Specs) using Mg Kα radiation ($\hbar\omega$=1253.6 eV). The X-ray power was 250 W. The spectra were recorded in the constant analyser energy (CAE) mode with analyser pass energies of 40 eV for the survey spectra and 20 eV for the high resolution ones. Charging effects were corrected by energy calibration on C 1s level relative to 284.5 eV. The base pressure in the analysis chamber during analysis was $3 \cdot 10^{-10}$ mbar.

DLS and Zeta-potential

Dynamic Light Scattering (DLS) and Zeta-potential experiments were carried out at 25°C on a Malvern Zetasizer Nano-ZS, equipped with a helium–neon 633 nm laser and Non-invasive Back Scatter (NIBS) optics/detector at 173°. The size distribution was calculated using a built-in auto-correlation function, whereas Zeta-potential was estimated by means of the M3-PALS (Phase Analysis Light Scattering) technique, measuring the particle electrophoretic mobility in a thermostated cell.

SLS

Static Light Scattering (SLS) spectra were recorded with a Horiba Jobin-Yvon Fluoromax 4 spectrofluorimeter equipped with a 150W Xenon arc lamp, by using a synchronous scan of the emission and excitation monochromators (scan range 200-800 nm) and a right angle geometry for excitation and photon detection.

Sonication process

In all the samples used the sonication conditions such as the ultrasound frequency and the effective energy density transferred to the GO sheet (i.e. energy/mass) were constant.

For a typical ultrasonic power output of 120W and frequency 37 kHz, the corresponding wavelength of sound (λ) in water was ca. 4 cm. The peak pressure in the wave was of the order $\Delta P \approx 1$ atm corresponding to a net stress applied to GO sheets of the order of $\Delta P(\text{size}/\lambda) \sim$ mPa, which induces the sheet breakdown.

Transmission Electron Microscopy (TEM) characterization of GO nanosheets deposited on metallic grids (fig. S1) showed a wrinkled structure typical of GO that, especially for the larger ones, does not allow an objective estimation of their size. See ref. [3] for more details.

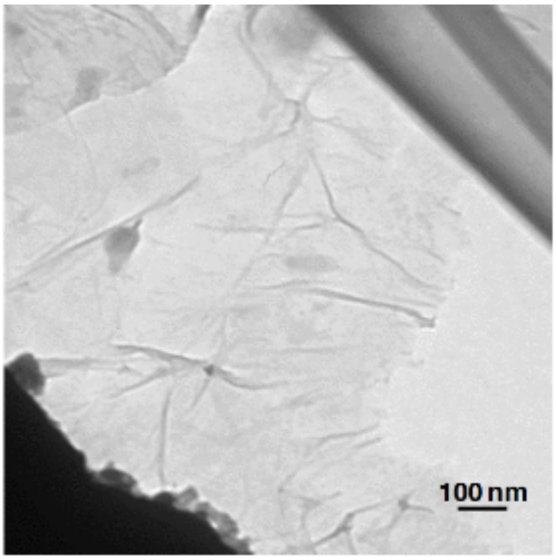

Fig. S1 TEM images of GO sheets. Samples (50 µg/ml) were deposited on copper grids prior to TEM observation. Reproduced from ref. [3]

2.IMAGE PROCESSING

Definition of image

Each FM, SEM and AFM image was treated as a matrix *A(i,j)*, where (i,j) was the 2D-position of each data-point. Each cell of the matrix for AFM images contained the height value (z). SEM and FM matrix cells contained instead the intensity of electrons and photons flux respectively.

Flattening procedure of an AFM image

Raw-data AFM images are affected by artefacts due to piezo scanning. Piezo-electric motors are commonly used to move the samples in sub-nanometric steps in all the Cartesian directions (X,Y,Z). For the sake of simplicity, we use the laboratory reference system (i.e. X,Y plane defined by the surface sample and Z perpendicular). In general, the in-plane movements *(x,y)* are decoupled, but Z-motion depends on in-plane position: $z = z(x,y)$. This means that the original data recorded into an AFM image of a flat surface are described by a 2D-hypersurface $z = f(x,y)$ instead of a plane $z = z_0$. Thus, the original AFM data have to be processed and the mathematical transformations applied to the image in order to minimize the artefacts are called “flattening procedures”.

The histogram distribution is a graph plotting for each height z the (normalized) number of points of the image having that height. It is one of the most suitable parameters to monitor the flattening procedure. In particular, the histogram curve Fc allows correction of the image slope because the histogram is the best indicator of the flatness of the surface. Plane surfaces are characterized by high and narrow histogram peaks and the peak width corresponds to the surface roughness in the case of a Gaussian distribution.[4]

A simple scheme is shown in Fig. S2 where (a), (b) and (c) represent the raw image, an intermediate and the correct image, respectively. Each step of the flattening procedure is monitored by evaluating the histogram distribution (displayed below each image). In particular, Fig. S2 shows the AFM image of GO sheets on silicon substrate at 20 hours sonication.

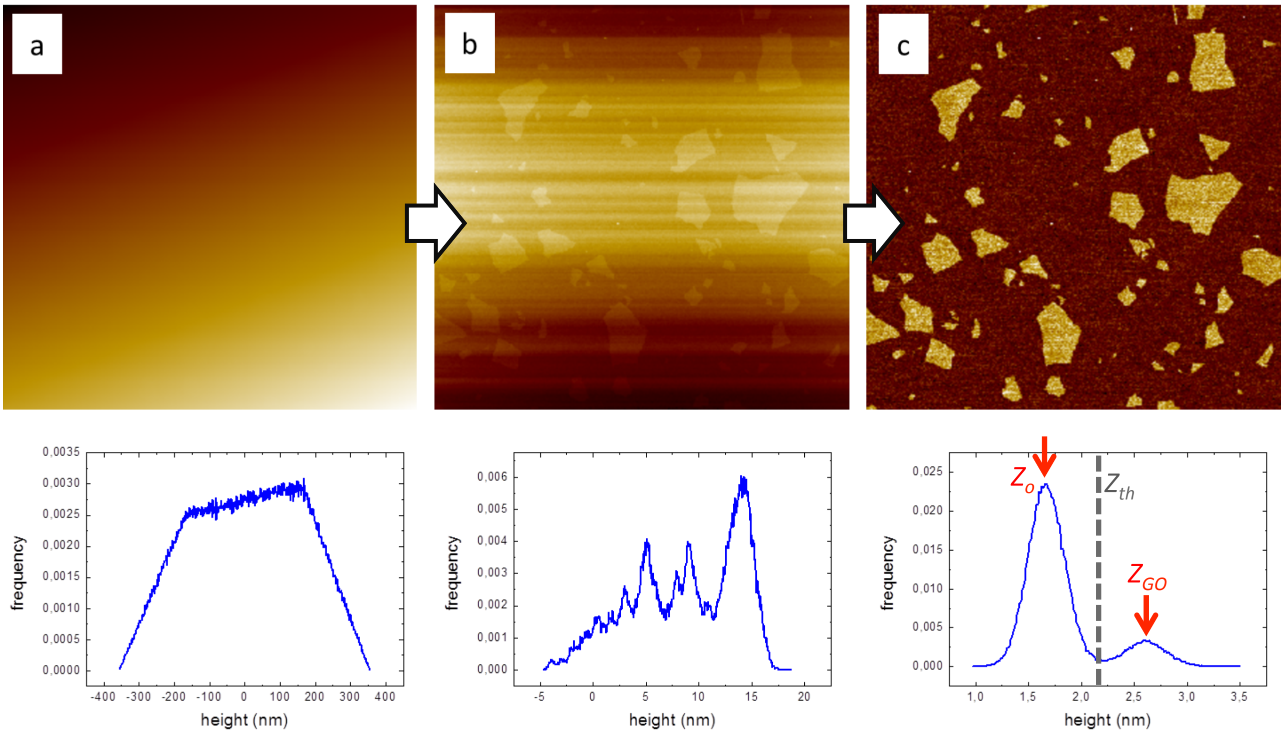

Fig. S2. Example of the flattening procedure. Corresponding height histograms are reported below each image. Red arrows indicate the substrate Z level (z_0) and the GO height (z_{GO}).

The correct (a.k.a. flattened) AFM image presents a symmetric histogram distribution well described by a Gaussian function. The peak width amounts to 3.80 ± 0.02 nm as calculated following the work of Olive et al.[5]

Automatic size analysis

After the flattening procedure (fig. S3A), bare substrate and GO sheets can be unambiguously distinguished by using a threshold value (z_{th}) defined as the mean value between the substrate Z level (z_0) and the GO height (z_{GO}): $z_{th} = (z_0 + z_{GO})/2$.

All the pixels (i,j) having the corresponding z value higher than the threshold are assigned to the GO sheets while the others are assigned to the substrate.

In this way, the image analysis software recognized all the GO sheets (depicted in fig. S3B, marked with different colours), counted them and calculated several morphological parameters such as area, size, perimeter, Aspect Ratio and Form Factor.

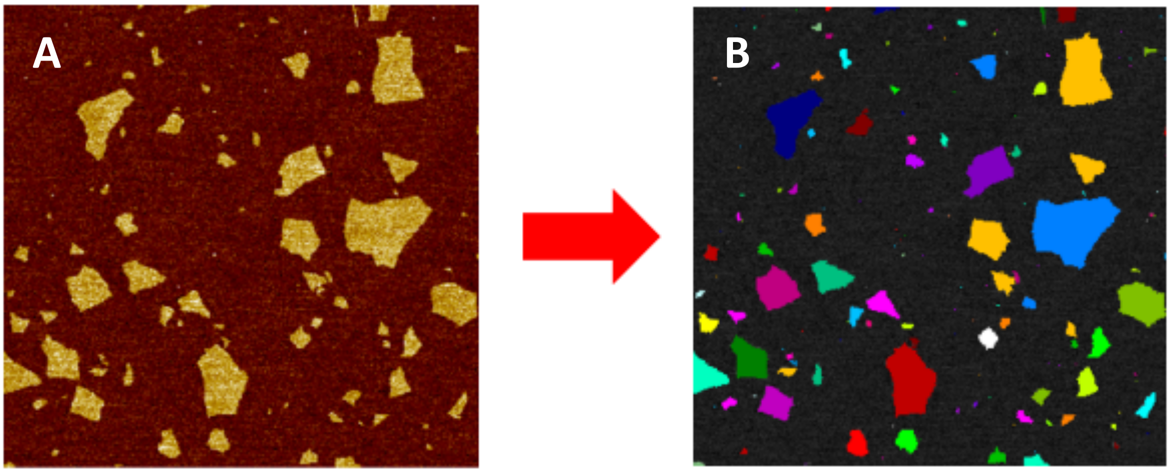

Fig. S3. A) Original AFM data and B) corresponding processed image where the GO sheets have been automatically identified by the software and marked with different colors.

Statistical parameters

Using the automatic image analysis, each image is decomposed into a set of elements. Each of them corresponds to a GO sheet and is defined by an array of six parameters: four used to describe the lateral size and two to describe the shape of the sheet.

Fig. S4 summarizes the information related to a single GO sheet with the size parameters such as:

- *Area* defined as the number of pixels occupied by the sheet on the surface (green region in Fig. S4B)

- *Size (s)* defined as the side length of the square having the same area of the sheet (white square in Fig. S4B)
- *Perimeter* defined by the length of outer contour (green contour in Fig. S4C)
- *Length (L)* defined as the distance between the two farthest pixels of each sheet (red line in Fig. S4C)

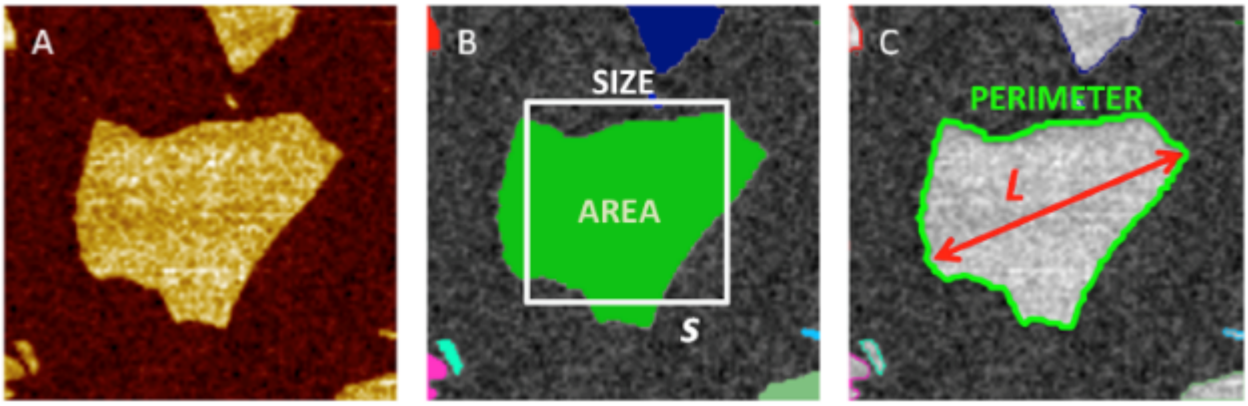

Fig. S4. Size parameters of GO sheet. A) AFM image, B) automatic recognition of GO area (green region) and corresponding C) perimeter (green line) and length (L).

For the quantitative analysis of the shape of the 2D objects, we focussed our attention on two dimensionless parameters:

- the *Aspect Ratio (A_R)*, namely the squared length divided by the area ($A_R = L^2/A$). This parameter describes the anisotropy of the shape considered, A_R is always ≥4/π (=4/π for circles and =2 for squares).
- the *Form Factor (FF)*, which combines area and perimeter ($FF = 4\pi A/p^2$), describing the shape irregularity: FF is always ≤1 (=1 for circles and =π/4 for squares).

Pixel resolution – overlapping

Image resolution basically depends on two independent factors: the lateral resolution of the experimental measurement and the pixel dimension (D_p) (a.k.a. pixel resolution). The first factor is related to the experimental parameters such as the physical properties of the probe-sample system. Conversely, the pixel resolution, defined as the ratio between the lateral size of the acquired image and the number of pixels: $D_p = size_{image}/N_p$, can be easily tuned. The chosen pixel dimension has to be much lower than the lateral size of the GO sheet in order to minimize the artefacts due to pixelization of the acquired image.

All the topographic images acquired using FM, SEM and AFM, are obtained by scanning areas within the range between 1 µm and 500 µm. In order to compare all the collected images, we chose different pixel resolutions, as shown in fig.S5, overlapping the values for the different techniques. The issue related to the pixelization was minimized by using an iterative procedure to find the suitable pixel dimension.

For each scanned area we *i)* acquired images with different D_p values, *ii)* obtained the corresponding area distributions and *iii)* calculated the average characteristic size $\langle s \rangle = \sqrt{\langle A \rangle}$.

We chose the pixel resolution value so that it was about 10 times lower than the average size of the measured GO sheets: $D_p \lesssim \langle s \rangle/10$.

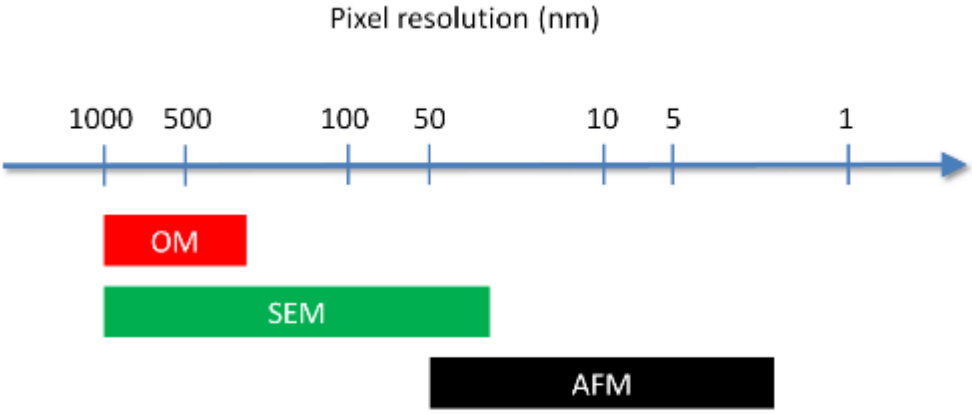

Fig. S5. Pixel resolution of all the acquired images.

3.MATHEMATICAL METHODS

Discrete distributions, operative definitions

After collecting all the images, we calculated for any studied parameter (*x*) a discrete probability distribution of the sheets f_x defined as the sheet distribution normalized for the total number of sheets. In general, a distribution is described using the mean value (<x>) and the corresponding standard deviation (SD), calculated as:

$$\langle x \rangle = \sum_{x_{min}}^{x_{max}} x_i \cdot f_x \ ; \qquad SD = \sqrt{\sum_{x_{min}}^{x_{max}} (x_i - \langle x \rangle)^2 \cdot f_x} \qquad \text{with } \sum_{x_{min}}^{x_{max}} f_x = 1.$$

These definitions can be generalized for the continuous distributions $f(x)$ where x is a continuous random variable:

$$\langle x \rangle = \int_{x_{min}}^{x_{max}} x_i \cdot f(x)dx \ ; \qquad SD = \sqrt{\int_{x_{min}}^{x_{max}} (x_i - \langle x \rangle)^2 \cdot f(x)dx} \qquad \text{with } \int_{x_{min}}^{x_{max}} f(x)dx = 1.$$

In the case of a Gaussian distribution, <x> and SD correspond to the position (a.k.a. mode) and the peak-width of the distribution respectively. Conversely, in the case of skewed distributions this simple relationship is not valid, as <x> and SD are given by a combination of the mode and the breadth of the distribution. In the case of highly skewed distributions, the standard deviation cannot be a useful parameter because it is larger than the mean value. This is a common issue related to the breadth and shape of the distributions that are usually determined most efficiently with parameters derived from the *higher* moments of the distribution. A detailed description can be found in [6].

<x> and SD are not sufficient to describe the given distribution. Fig. S6, as example, shows two different discrete distributions f_x: (red) Gaussian and (blue) scattered bimodal, having the same pair of statistic parameters <x> and SD. Both distributions are normalized.

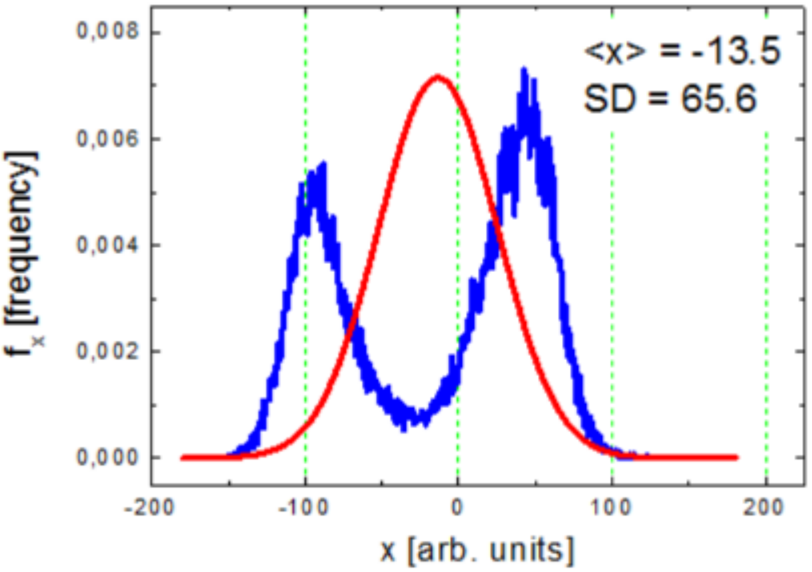

Fig. S6. Two distributions described by the same pair of statistical parameters: <x> and SD.

For the sake simplicity, in the main text we used indistinctly the words “distribution” and “function”.

Choice of the “optimal” number of sampling points to reconstruct the distribution

The number of bins *Nb* used to build the size distribution histogram is calculated as the ratio between the x-range and the bin width h:

$$Nb = \left[\frac{x_{max}-x_{min}}{h}\right]$$

where min (max) value corresponds to the smallest (largest) measured sheet, while the braces indicate the ceiling function.

The parameter h is a smoothing or localizing parameter and controls the width of the histogram bins. A value of h that is too large leads to very big blocks and thus to a very unstructured histogram. On the other hand, when the h value is too small it gives a very variable estimate with many unimportant peaks. The choice of the "optimal" value is not trivial and several methods are suggested.[7] We used the Scott's rule: $h = 3.49 \cdot SD \cdot n^{-1/3}$, because it is simple and well-founded in statistical theory, taking into account the SD of the acquired dataset as well as the number of measured sheets (n).[8]

Sampling

Managing macroscopic samples and solutions requires treating systems with an enormous number of objects. For example, if we consider 1 g of single layer graphene sheets with a mean area of 10 μm^2, the entire population corresponds to about 10^{14} objects. It is not possible to manage such quantities and for this reason, the system has to be treated with statistical approaches.

What is the minimum number of GO sheets from within a statistical population to estimate the characteristics of the entire GO solution?

We faced this problem by monitoring how the area distribution changes with an increasing number of GO sheets (N_{sheet}) measured by different microscopy images. When the area distribution no longer changes (i.e. asymptotic behavior), the corresponding N_{sheet} value is the representative sample of the GO solution.

In particular, we monitored three parameters to quantify the change of shape of the distribution f_x:

- Skewness (the measure of the f_x asymmetry): $ske = \frac{\langle x^3 \rangle - 3 \cdot \langle x \rangle \cdot SD^2 - \langle x \rangle^3}{SD^3}$

- Kurtosis (the measure of the f_x tailedness): $ku = \frac{\langle x^4 \rangle}{SD^4}$
- Tail percentage: $tail = \frac{N_{tail}}{N_{sheet}}$, where the first N_{tail} value corresponds to the root square of the number of sheets (Poisson distribution).

The evolution of these three parameters is reported in Fig. S7 for the case of 2 sonication hours. We acquired 14 images (AFM and SEM), corresponding to about 3,500 sheets. All the three parameters tend to an asymptotic value for N_{sheet} larger than 2,500.

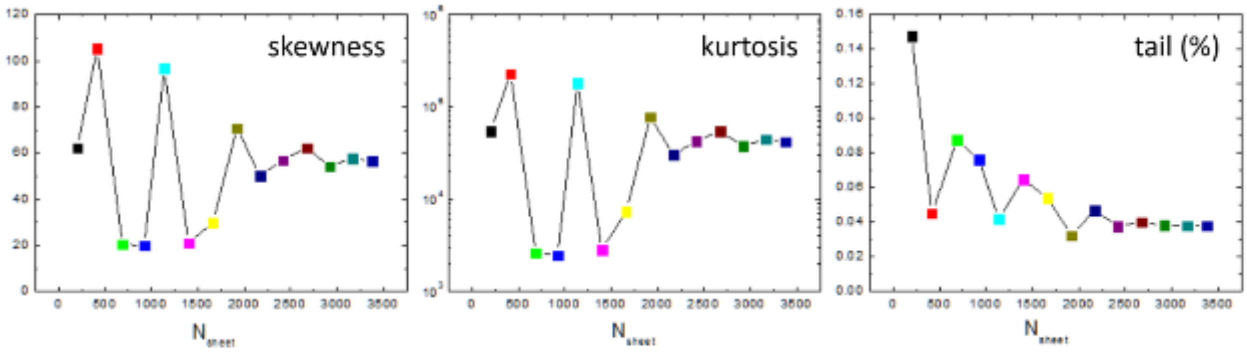

Fig. S7. Fitting analysis. Evolution of the shape of area distribution.

Thus, we are confident that 2,500 is the minimum number of GO sheets from within a statistical population to estimate characteristics of the GO solution at 2 sonication hours.

The same procedure has been repeated for all the sonication times and corresponding N_{sheet} values range between 2,000 and 3,000.

List of analytic continuous distributions used

All the acquired area distributions were fitted with the probability distributions commonly used in fragmentation models:[9] Inverse power, Log-normal, Gamma and Exponential functions.

- Inverse power law describes a scale invariant (a.k.a. fractal) fragmentation, depicting a series of fragmentation processes that do not depend on the size of the fragment.
- Log-normal distribution describes random fragmentation processes with a random distribution of the fragment shape, and has previously been used to describe many rock crushing processes and fragmentation of 2D materials.[10]
- Gamma function describes the fragment distributions following a particular partition of Euclidean surfaces called Voronoi tessellation.[11] Because Gamma and Log-normal functions have very similar shapes they are often used indiscriminately, despite describing different mechanisms.
- Exponential functions (a.k.a. Mott functions) describe from a purely statistical point of view fragmentation given by randomly oriented cracks.

The mathematical functions mentioned in the main text are listed below:

Table S1. List of the analytic distributions and the corresponding mean and SD.

Distribution	Equation	$\langle x \rangle$	SD
Gaussian	$\frac{1}{w\sqrt{2\pi}} \cdot e^{-\frac{(x-x_0)^2}{2w^2}}$	x_0	w^2
Log-normal	$\frac{1}{xw\sqrt{2\pi}} \cdot e^{-\frac{(lnx-x_0)^2}{2w^2}}$	$e^{x_0+w^2/2}$	$\left(e^{-w^2}-1\right) \cdot e^{2x_0+w^2}$
Gamma	$\Gamma(\alpha) \cdot x^{\alpha-1} \cdot e^{-\beta x}$, $\alpha, \beta > 0$	$\frac{\alpha}{\beta}$	$\frac{\alpha}{\beta^2}$
Power law	$\frac{1}{x^{\alpha}}$	-	-
Mott	$e^{-\gamma \cdot \sqrt{x}}$	-	-

The Gaussian function is a symmetric distribution where the mean value corresponds to the median and the mode, i.e. the position of the peak. The statistical parameters are calculated within the domain $x \in \Re$. All the other functions are asymmetric and defined for positive variables. The statistical parameters of Log-Normal and Gamma functions are calculated within the domain $x \in (0, +\infty)$.

Data fit

In general, discriminating between different asymmetric distributions is not simple (see ref. [12] as an example). In order to tackle this well-known problem, we studied the complementary *cumulative distribution functions*: $CCD(\xi) = 1 - \int_0^{\xi} f(x)dx$ together with the distribution itself *f(x)*. This function can be defined both for discrete and continuous distributions.

For example, taking into account our experimental dataset, given a certain area value (A_i), the CCD(A_i) function indicates the population of GO sheets larger than A_i. For this reason it is also called the *survival* or *reliability* function.

Fig. S8 reports the study performed on (A) the area distribution and (B) the corresponding CCD of GO sheets after 20 sonication hours, comparing the best-fit functions obtained by using the Levenberg–Marquardt algorithm corresponding to (purple) Log-normal, (red) Gamma and (green) Mott distributions. The corresponding χ^2 coefficients are reported in table S2 (the lower χ^2, the better the fitting).

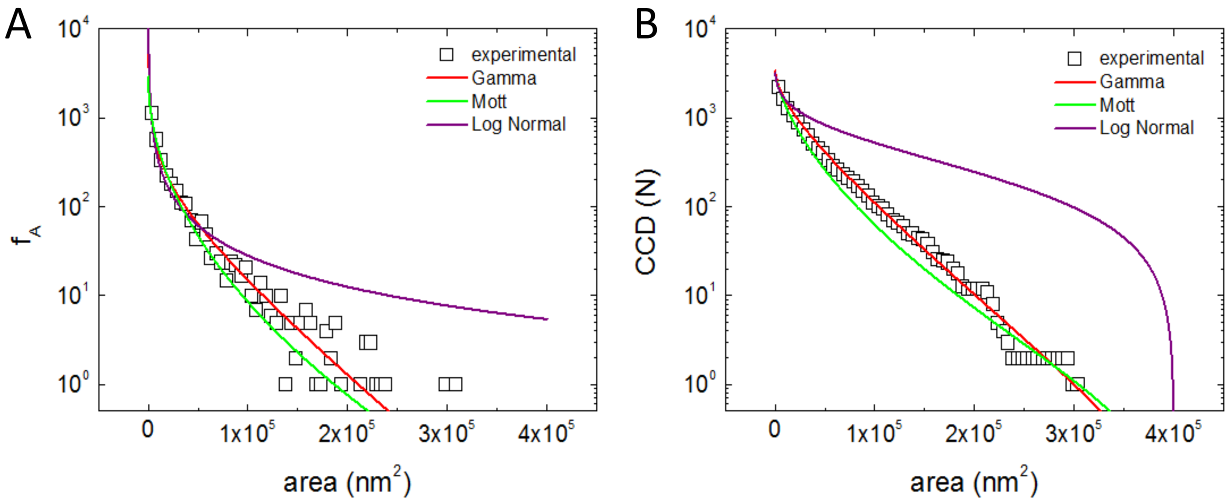

Fig. S8. Fitting analysis. (A) Distribution of GO sheets after 20 sonication hours and (B) the corresponding cumulative distribution function. The experimental distributions are fitted with (purple) Log-normal, (red) Gamma and (green) Mott distributions.

Table S2. χ^2 *coefficients of best-fit.*

	$f(area)$	$CCD(area)$
Log-normal	39.6	13093
Gamma	9.15	126.6
Mott	16.6	1139.7

The χ^2 coefficient of the Gamma function is the lowest, clearly demonstrating that this function better reproduces the measured dataset.

This procedure has been used for all the area distributions acquired at all the different sonication times. Gamma distribution always shows the lowest χ^2 coefficient in the range between 0.5 hours and 40 hours sonication times.

It is noteworthy that the statistical analysis has been performed for all the statistical parameters taken into account, such as area, size, perimeter, Form Factor and Aspect Ratio.

Time-evolution of the shape of GO sheets

In the main text, we evaluated the shape of GO sheets for different sonication times by monitoring the Form Factor (FF) statistical parameter. The experimental results suggested the presence of the GO populations (P_G and P_E) with different shape which did not change during sonication. This picture has been confirmed by analyzing further shape parameters such as the Aspect Ratio (A_R), described before (see Fig. S9).

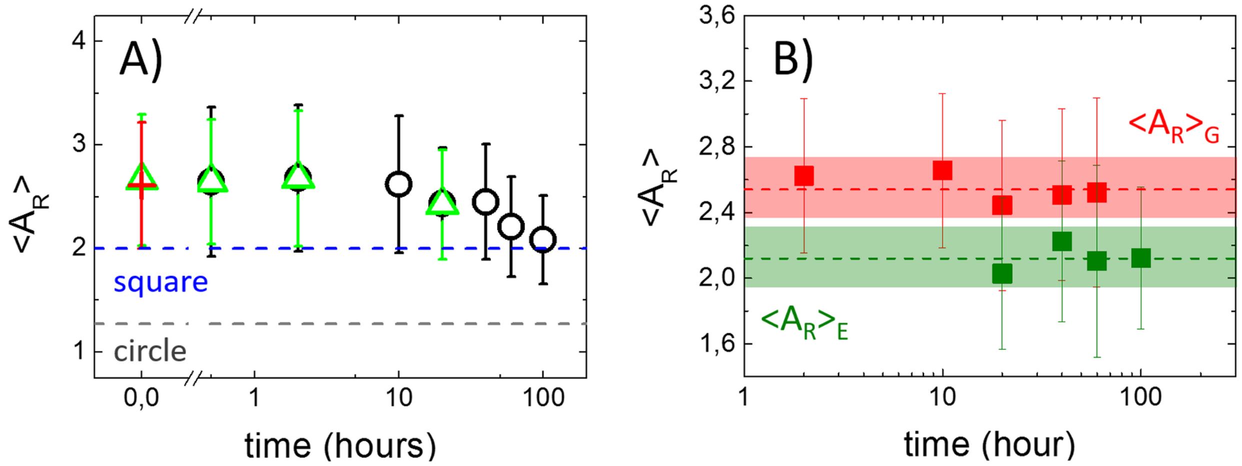

Fig. S9. Time-evolution of the Aspect Ratio parameter of GO sheets: (A) mean value and SD and (B) monitoring the two populations: (red squares) P_G and (green circles) P_E using the f_A analysis. Dashed lines correspond to $<A_R>_G$ and $<A_R>_E$ values. Shadowed areas are centered to the corresponding average values of the shape parameters (dashed lines) and the widths correspond to twice the standard deviation (= 2·SD).

4.CHEMICO-PHYSICAL ANALYSIS

Monitoring of C/O ratio of the GO sheets

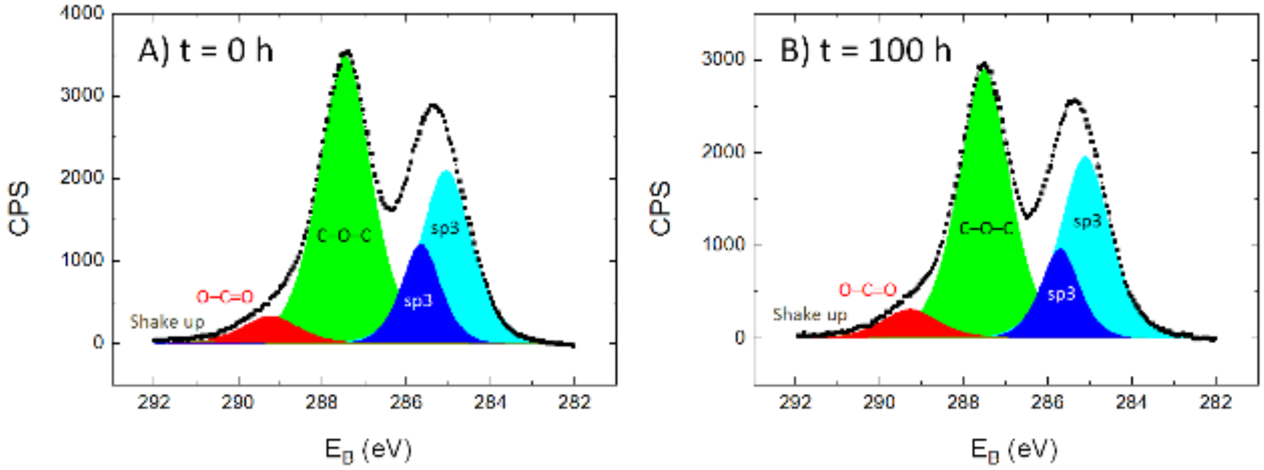

Fig. S10. XPS surveys. High-resolution core level spectra Carbon 1s of GO sheets before (A) and after (B) 100 hours of sonication. XPS spectra have been corrected by removing the background.

The high-resolution C1s XPS spectra exhibited contributions of different C-C bonds and the presence of hydroxyl and carboxyl groups. In particular, we distinguished five components at 284.4 eV (C sp2), 285.0 eV (C sp3), 286.8 eV (C-O-C) 288.5 eV (O-C=O) and 290.8 eV (shake-up).

All the XPS spectra were obtained by subtracting the Shirley background (as displayed in Fig. S10) and then fitted with a Voigt function for each component. The Full Width Half Maximum value of all the five components is between 1.0 and 1.6 eV. We analyzed three samples for each sonication time.

The oxidation degree of the GO sheets (C/O) (i.e. the ratio between the number of oxygen and carbon atoms: C/O) was calculated as a combination of the measured contribution weight by the area (A_x):

$$C/O = \frac{A_{sp2}+A_{sp3}+A_{C-O-C}+A_{O=C-O}}{A_{C-O-C}/2+2\cdot A_{O=C-O}}\,.$$

The areas of all the contributions obtained by the fit procedures are reported in the table S3.

The analysis of the relative contributions shows that the chemical functional groups as well as the amount of carbon chemical species (*sp*^{2}- for graphitic clusters and *sp*^{3} for the defects) did not change significantly. The corresponding C/O ratio amounts to 2.4 strongly indicating that the chemical properties of the GO sheets were not modified by the long sonication treatment.

Table S3. Relative composition of C1s spectra.

	C sp2	C sp3	C-O-C	O=C-O	C/O ratio
0 hours	29±2	13±1	52±1	6±1	2.38±0.08
100 hours	32±2	12±1	50±1	6±1	2.42±0.08

Zeta-potential analysis

GO sheets are typically functionalized with hydroxyl groups and carboxyl groups, which bear a different amount of negative charges depending on sheet composition and pH.[13] All the samples produced showed a Z-potential of -50 ± 29 mV, independent of GO size (Fig. S11) confirming that: *i)* the sheets are strongly solvated, do not interact with each other in the solution and *ii)* the number of charged chemical groups present on their surface is constant. The first point confirms the long stability of the solutions observed experimentally, while the second one indicates that the chemical properties of the GO sheets do not vary with the lateral size.

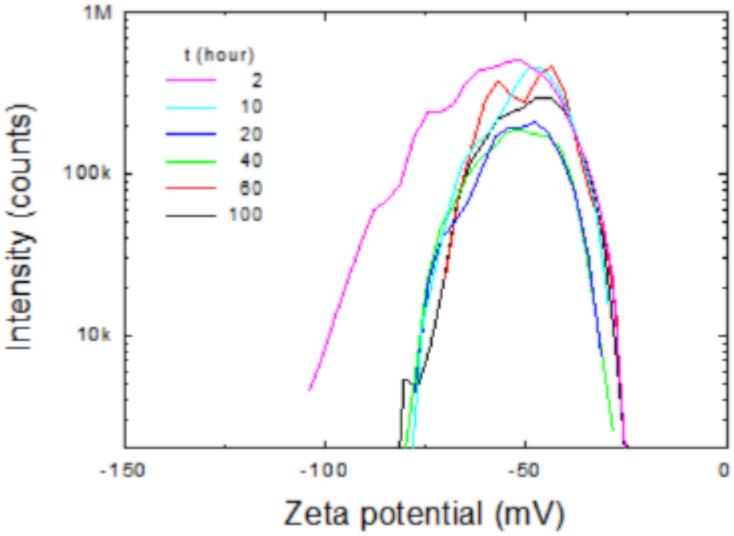

Fig. S11. Zeta potential spectra of GO in water solution acquired for different sonication times.

5.PHYSICAL MODELLING

2D fragmentation – Scaling properties

The geometry of fragments clearly influences the fragmentation processes, which is reflected in different behaviors of the time-dependence of the mean values of the area <A> and of the characteristic size <s>. According to the Cauchy–Schwarz inequality,[14] it is simple to demonstrate that the ratio of these two parameters differs from unity: $\langle A\rangle/\langle s\rangle^2 \neq 1$. Using a random scission model, Krapivsky et al.[15] demonstrated the scaling behavior of the 2D fragmentation showing that the ratio depends asymptotically on time: $\langle A\rangle/\langle s\rangle^2 \sim t^{-n}$, where $n = \sqrt{17} - 4 \cong 0.123$.

Fig. S12 shows how the ratio varies with increasing sonication time. Values are calculated directly from the experimental data (fig. 2A) and taking into account the equation $\langle s\rangle = \langle\sqrt{A}\rangle$. The ratio values decrease linearly in log-log scale with a slope of 0.13±0.01 showing an excellent agreement with theory. This evidence strongly indicates that the GO fragmentation is a 2D random scission which does not affect the shape of the fragments.

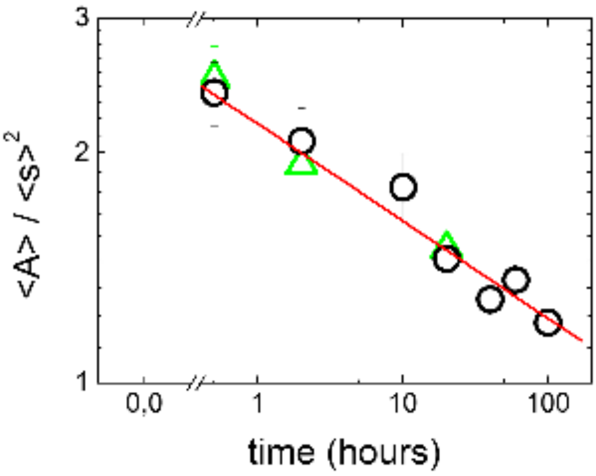

Fig. S12. Time evolution of $\langle A\rangle/\langle s\rangle^2$ ratio calculated by (+) FM, (△) SEM and (○) AFM.

The experimental trend strongly indicates that the fragmentation of GO is a homogeneous processes[16] in which the shape of the fragment does not change with time.

It is noteworthy that this picture has been developed by calculating the area (and size) of all the GO sheets without any analysis of the area distribution. A more correct analysis, performed taking into account the two populations, is reported in main text. Fig. S13 shows a cartoon schematizing the different fragmentation mechanisms acting on different scales.

Scheme of fragmentation processes

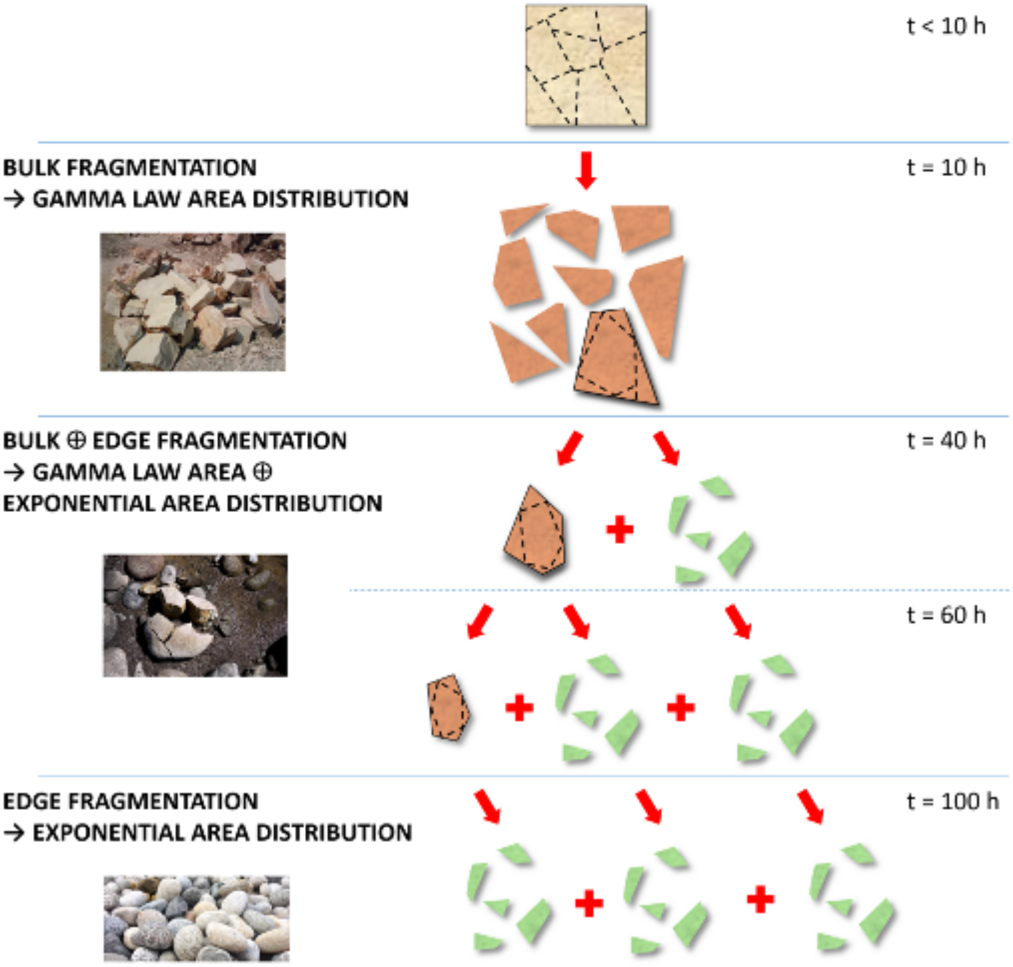

Fig. S13. Schematic representation of the different fragmentation mechanisms between 10 and 100 sonication hours, observed together with some every-day examples of rock fragmentation.

Bulk fragmentation - Modelling of the cavitation shear stress

XPS and Zeta-potential measurements confirm that the sonication did not affect the chemical properties of the GO sheets in solution. For this reason, any change in fragmentation mechanism was only due to the smaller size of the GO sheets involved. During sonication, the implosion of the cavitation bubbles created in the liquid imposes an inward radial fluid flow, which induces viscous forces on the graphene sheets that can thus fracture. After multiple fractures, fragments are generated with an asymptotic area ($<A>_G$) corresponding to the smallest surface on which the viscous stress cannot generate a lateral force high enough to further break of the fragment.

Here we extend to GO sheets the approach proposed for nanotubes by Ahir et al.[17] If a bubble of radius R implodes at a velocity $\dot{R}$, the mass conservation law $4\pi R^2 dR = 4\pi x^2 dx$, where x is the radial coordinate, implies a fluid velocity in the form $v(x) = R^2\dot{R}/x^2$. The GO sheet is described by a characteristic lateral size s and a thickness h, as summarized in the Fig. S14.

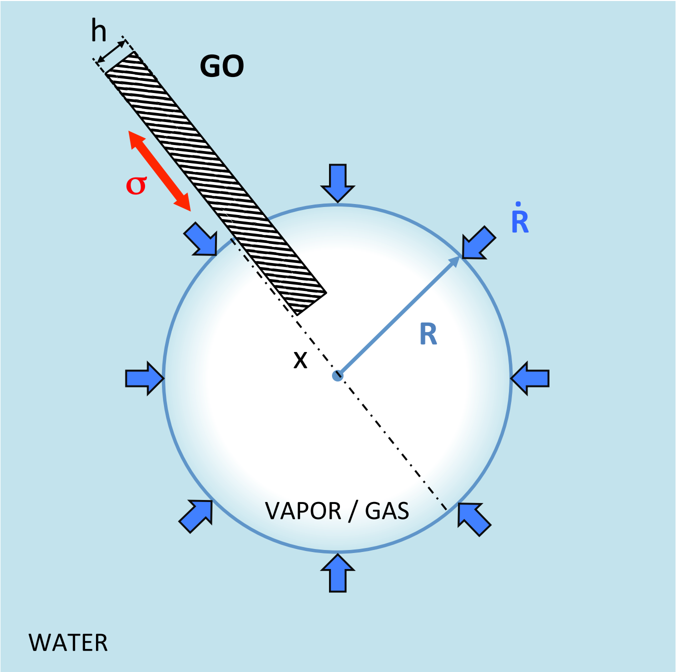

Fig. S14. Scheme of the collapsing bubble.

We define the *stagnation point* as $v(x_0) = V$, which can be calculated by balancing the viscous force F along the sheet, placed between xx_1 and $x_2 = x_1 + s$, according to $F = \eta \frac{L}{h} \int_{x_1}^{x_0} [v(x) - V] dx = \eta \frac{L}{h} \int_{x_1}^{x_2} [V - v(x)] dx$, where $x_0 = \sqrt{x_1 x_2}$.

The self-equilibrated two forces acting on both the sides of the graphene can be written as

$F = \eta \frac{L}{h} \int_{x_1}^{x_0} [v(x) - V] dx = \eta \frac{L}{h} R^2 \dot{R} \left(-\frac{1}{x} - \frac{1}{x_0^2} \right) \Big|_{x_1}^{x_0} = \eta \frac{L}{h} R^2 \dot{R} \left(\frac{1}{x_1} + \frac{1}{x_2} + \frac{1}{x_0} \right)$.

It is noteworthy that both faces of the sheet feel the viscous shear stress (dividing by $A = s \cdot h$ and multiplying the force for a factor 2). The corresponding applied viscous normal stress can be written as:

$$\sigma_\eta = \frac{2\eta R^2 \dot{R}}{h^2} \left(\frac{1}{x_1} + \frac{1}{x_1 + s} - \frac{2}{\sqrt{x_1 (x_1 + s)}} \right) \tag{1}$$

The maximal stress is reached at the smallest distance $x_1 = R$:

$$\sigma_\eta^{(\max)} = \frac{2\eta R^2 \dot{R}}{h^2} \left(\frac{1}{R} + \frac{1}{R + s} - \frac{2}{\sqrt{R (R + s)}} \right) \tag{2}$$

Eq. (2) calculates the maximal normal stress that can act to the GO sheet. This value cannot exceed the fracture strength of the GO: $\sigma_f^{(GO)}$. Thus, for a given characteristic size *s*, the sheet fragmentation complies with the equation:

$$\sigma_\eta^{(\max)} \le \sigma_f^{(GO)} \tag{3}$$

The asymptotic size of the GO sheet can be calculated using the eq. 2, for the case $R \gg s$:

$$s_{asy,GO} \approx h \sqrt{\frac{2R\sigma_f^{(GO)}}{\eta \dot{R}}} \tag{4}$$

Taking into account that the sheet area is the square of the characteristic size: $s = \sqrt{A}$, we describe the fracture strength of the GO sheet as:

$$\sigma_f^{(GO)} \approx \frac{\eta \dot{R}}{2R} \cdot \frac{\langle A \rangle_G}{h^2} \tag{5}$$

where the first factor describes the dynamics of the collapsing bubble in terms of stress rate ($\dot{R}/R \approx 10^9$ s^{-1}) and water viscosity.[18] The second factor is related to the morphology of the GO fragment, where h is the thickness and $\langle A \rangle_G$ is the asymptotic area of the GO population obtained by "bulk fragmentation" and following the Gamma area distribution, as shown in fig. 4 in the main text. The dynamics of the collapsing bubble (radius and velocity) have been calculated by solving the Rayleigh-Plesset equation using the adiabatic approximation (k = 1.4), considering the gas as non-condensable and neglecting the thermal and surface tension effects. A detailed description can be found in the book by Brennen (chapter 3) and references therein.[19]

Edge fragmentation mechanism

The mechanical stress of cavitation acts directly and indirectly on the rupture mechanisms of the GO sheets in solution. A simplified scheme is reported in Fig. S15.

Large fragments are directly generated by the mechanical stress of cavitation, as modelled in the previous section. Stress creates large cracks in pristine sheets (fig. S15A) leading to the formation of "bulk fragments" (i.e. first generation of fragments, following a Gamma size distribution).

A further mechanism has to be taken into account because unstable cracks can branch off from the main crack that generates the bulk fragments (fig. S15B).[20] This mechanism is responsible for additional edge erosion of the first generation fragments. After 100 hours sonication, bulk fragments are completely eroded leading to a new population of small GO sheets (<s> ≈ 45 nm) whose area distribution follows an exponential curve (second generation of fragments, fig. S15D).

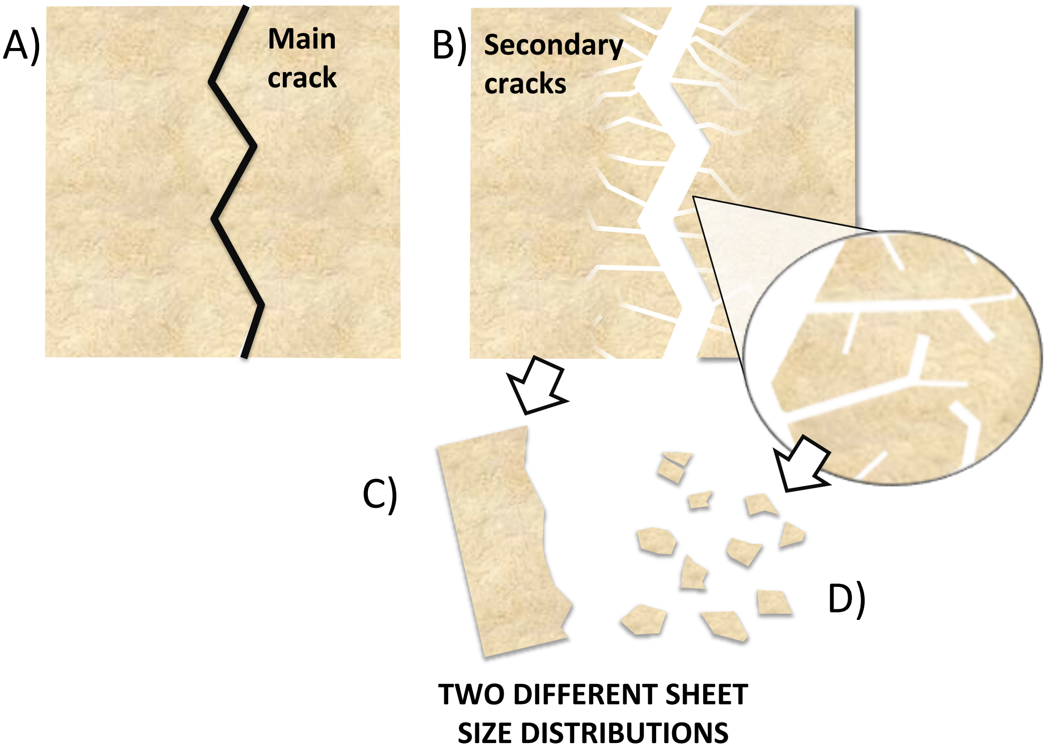

Fig. S15. Scheme of fragmentation mechanisms.

Bibliography

1 Treossi, E. *et al.* High-Contrast Visualization of Graphene Oxide on Dye-Sensitized Glass, Quartz, and Silicon by Fluorescence Quenching. *J Am Chem Soc* **131**, 15576, doi:Doi 10.1021/Ja9055382 (2009).

2 Liscio, A., Palermo, V. & Samorì, P. Nanoscale Quantitative Measurement of the Potential of Charged Nanostructures by Electrostatic and Kelvin Probe Force Microscopy: Unraveling Electronic Processes in Complex Materials. *Accounts Chem Res* **43**, 541-550, doi:10.1021/ar900247p (2010).

3 Russier, J. *et al.* Evidencing the mask effect of graphene oxide: a comparative study on primary human and murine phagocytic cells. *Nanoscale* **5**, 11234-11247, doi:10.1039/c3nr03543c (2013).

4 Liscio, A. Scanning Probe Microscopy beyond Imaging: A General Tool for Quantitative Analysis. *Chemphyschem* **14**, 1283-1292, doi:DOI 10.1002/cphc.201200880 (2013).

5 Oliver, R. A. Advances in AFM for the electrical characterization of semiconductors. *Rep Prog Phys* **71**, doi:Artn 076501 Doi 10.1088/0034-4885/71/7/076501 (2008).

6 DeCoursey, W. J. *Statistics and probability for engineering applications with Microsoft Excel*. (Newnes, 2003).

7 Härdle, W. & Simar, L. *Applied multivariate statistical analysis*. (Springer, 2003).

8 Scott, D. W. OPTIMAL AND DATA-BASED HISTOGRAMS. *Biometrika* **66**, 605-610, doi:10.1093/biomet/66.3.605 (1979).

9 Zhang, F. *Shock wave science and technology reference library*. (Springer, 2009).

10 Monteiro, M. J. Fitting molecular weight distributions using a log-normal distribution model. *Eur Polym J* **65**, 197-201, doi:10.1016/j.eurpolymj.2015.01.009 (2015).

11 Okabe, A., Boots, B. N. & Sugihara, K. k. *Spatial tessellations : concepts and applications of Voronoi diagrams*. (Wiley, 1992).

12 Kouroupis-Agalou, K. *et al.* Fragmentation and exfoliation of 2-dimensional materials: a statistical approach. *Nanoscale* **6**, 5926-5933, doi:Doi 10.1039/C3nr06919b (2014).

13 Dreyer, D. R., Park, S., Bielawski, C. W. & Ruoff, R. S. The chemistry of graphene oxide. *Chem Soc Rev* **39**, 228-240 (2010).

14 Hazewinkel, M. *Encyclopaedia of mathematics : an updated and annotated translation of the Soviet "Mathematical encyclopaedia"*. (Reidel ; Sold and distributed in the U.S.A. and Canada by Kluwer Academic Publishers, 1988).

15 Krapivsky, P. L. & Bennaim, E. Scaling and Multiscaling in Models of Fragmentation. *Phys Rev E* **50**, 3502-3507, doi:DOI 10.1103/PhysRevE.50.3502 (1994).

16 Bertoin, J. Homogeneous fragmentation processes. *Probab Theory Rel* **121**, 301-318 (2001).

17 Ahir, S. V., Huang, Y. Y. & Terentjev, E. M. Polymers with aligned carbon nanotubes: Active composite materials. *Polymer* **49**, 3841-3854, doi:10.1016/j.polymer.2008.05.005 (2008).

18 Hennrich, F. *et al.* The Mechanism of Cavitation-Induced Scission of Single-Walled Carbon Nanotubes. *The Journal of Physical Chemistry B* **111**, 1932-1937, doi:10.1021/jp065262n (2007).

19 Brennen, C. E. *Fundamentals of multiphase flow*. 1st pbk. edn, (Cambridge University Press, 2009).

20 Åström, J. A., Ouchterlony, F., Linna, R. P. & Timonen, J. Universal Dynamic Fragmentation in D Dimensions. *Physical Review Letters* **92**, 245506 (2004).